This manuscript is the accepted Pre-Print of the paper "*Kumar DM, Catrini P, Piacentino A, Cirrincione M. Advanced modeling and energy-saving-oriented assessment of control strategies for air-cooled chillers in space cooling applications, Energy Conversion and Management, 2023, Vol. 291, art. No. 117258, doi: 10.1016/j.enconman.2023.117258*"

Advanced modeling and energy-saving-oriented assessment of control strategies for air-cooled chillers in space cooling applications

Dhirendran Munith Kumar[1*], Pietro Catrini[1], Antonio Piacentino[1], Maurizio Cirrincione[2]

[1]Department of Engineering, University of Palermo, Viale Delle Scienze, Palermo, Italy.
[2]School of Information Technology, Engineering, Mathematics and Physics, University of the South Pacific, Fiji.
[*]Corresponding author's e–mail: dhirendranmunith.kumar@unipa.it

Abstract

Chillers are reference technologies to meet the demand for space cooling in the tertiary and commercial sectors. Meantime, being power-to-cold technologies, they could increase the flexibility of these buildings in those contexts of a high share of electricity from renewable energy sources through new control strategies. To reliably assess the achievable energy savings in these novel applications, models capable of simulating not only the steady-state operation but also the dynamic response are required. However, the operation of these systems is usually evaluated through highly simplified models, also omitting controls. To fill this gap, this paper proposes an integrated thermodynamic and control modeling for an air-cooled chiller, accounting for usual and innovative control strategies. To show the capabilities of the model, an air-cooled chiller serving an office in the Mediterranean area is assumed. Both a variable-speed chiller and a constant-speed chiller with sequential control for compressors are simulated. Results show that for a variable-speed chiller, the set point for the supplied cold water is met, and the thermal inertia of the hydronic loop affects the reaching of the steady-state operation. In the case of a constant-speed chiller with sequential control, the number of "ON-OFF" cycles for each compressor is monitored and the minimum inertia of the hydronic loop for the safe operation of compressors is found. The analysis reveals that a variable temperature setpoint for the supplied water allows for a percentage increase in the energy performance between 10.8%-60.3%. The proposed model enables the analysis of innovative controls aimed at improving energy savings and increasing building flexibility.

Keywords

Energy savings, air conditioning, space cooling, air-cooled chiller, thermodynamic modeling, control strategy, dynamic response.

1. Introduction

In 2021 space cooling accounted for nearly 16% of the building sector's final electricity consumption [1]. This share is expected to increase in the near future as climate change and population growth will push the demand for cooling [2]. The use of electricity from renewable energy sources (RES) together with the adoption of high-performance air-conditioning systems could limit the environmental effects of such an increase [3]. Focusing on air-conditioning systems, air-cooled and water-cooled chillers are widely adopted to meet the cooling demand in the tertiary and commercial sectors. To achieve higher energy savings, in the last two decades, traditional constant-speed systems have been gradually replaced by variable-speed technologies [4]. To further improve the energy and environmental performance, heat exchanger design has been improved [5], scroll compressors have gradually replaced reciprocating compressors [6], and new refrigerants with low global warming potential have been developed [7].

In addition to technological improvements, research has devoted great efforts to increasing the energy performance of these systems when operating in buildings. In this respect, several studies have proposed deterministic or stochastic approaches to determine optimal and robust operating strategies. For instance, Niu et al. [8] proposed a genetic algorithm to optimize the setpoint for water-cooled chillers in Shanghai (China). The results showed an 8.5% increase in energy savings. Chan et al. [9] used an artificial neural network together with particle swarm optimization to operate a chiller plant serving a hospital. The neural network predicted the outdoor temperature and building cooling demand, while the particle swarm optimization aimed at finding the optimal value setpoints for chilled water supply temperature. The author estimated an 8.6% increase in energy performance compared with the traditional control strategy. Catrini et al. [10] proposed exergoeconomics to optimize both the energy and economic performances of multiple air-cooled chillers. The minimum unit cost of the chilled water was achieved in the case of unevenly sized chillers. Saloux and Zang [11] developed a data-driven model-based control to vary the supply water temperature setpoint for a water-cooled chiller. The results pointed out a 33% reduction in electric energy consumption. Fan and Zhou [12] proposed a model-based predictive control to optimize the operation of water-cooled chiller plants with a water-side economizer. The authors estimated a 14.3% decrease in energy consumption compared to conventional control. Ismaen et al. [13] optimized the design and operation of multiple chillers in a district cooling network through multiple integer linear optimization, while considering chiller short-cycling and the unloading conditions. Zhang et al. [14] simulated the operation of an air-cooled chiller for cooling in data centers, and the relation among the power consumption with return water temperature, ambient temperature, and the water flow rate was investigated to minimize energy consumption. Qiu et al. [15] proposed a hybrid model-free chilled water temperature to reset the supply cold water temperature method for chillers is proposed. The method relied only on reinforcement learning techniques without needing preliminary modeling of components. The authors claimed that the approach could be a useful alternative for systems without sufficient data due to its online self-learning capability. Liu et al. [16] proposed a method for optimizing the operation of chillers in the presence of uncertainties in cooling demand by using a Markov chain. Results showed that confidence in the method could be increased by 56.7%. Sun et al. [17] developed a method based on the Monte Carlo technique to reduce the impacts of flow measurement uncertainties in the case of multiple chillers sequencing control. Alghamdi et al. [18] found that a proportional-integralderivative controller for a chiller with five temperature setpoints allowed for only a 2.2% increase in energy savings. Yu and Chan [19] proposed a method for determining optimum condensing temperature and variable chilled water flow for the case of air-cooled centrifugal chillers. Liao et al. [20] evaluated the robustness of typical chiller sequencing controls in the presence of uncertainties. The analysis revealed that some control strategies could contribute to the worsening of uncertainty levels.

Other research studies focused on developing advanced supervisory controls for chillers (and other cooling systems) to increase the so-called "building flexibility" (i.e., the capability of the building to adapt its operations not only to meet the needs of the occupants but also to help power grid operators in managing hours of high demand or surplus of electricity production from RES) [21]. In this respect, it is widely recognized that electrically driven cooling (and heating) systems could support the management of the power grid in the context of the high share of RES [22]. Indeed, by being activated in the presence of an electricity surplus, the produced cold can be stored onsite [23] or sold to a cooling network [24]. Moreover, by adopting demand-response strategies [25], loads of the served building could be shifted from peak to off-peak periods thus reducing stress on the power grid caused by high demand. For instance, Tina et al. [26] investigated the capability of commercial buildings in providing flexibility to help power grid operators. A Mediterranean shopping center served by a vapor compression system was assumed as a case study. The authors found that a large flexibility potential exists throughout the year, although occupants' discomfort could arise during summer. Lu et al. [27] investigated the achievable flexibility thanks to the integrated operation of cooling systems and building thermal mass in the case of nearly zero-energy office buildings. Compared with the traditional night set-back control, the peak demand can be reduced by about 55%. Mugnini et al. [28] evaluated the operational flexibility of the common residential space cooling technologies, paying particular attention to the distribution system. Results show that split systems show lower flexibility, whereas promising results could be achieved in the case of hydronic cooling systems. Triolo et al. [29] estimated cooling demand flexibility in a district energy system equipped with chillers achieved by using temperature set point changes. The authors estimated a 13.5% decrease in the demand in the case of a 1.1 °C setpoint increase.

In general, from the previous literature analysis, it was observed that some of the published papers usually relied on very simplified modeling of chillers [14],[13]. Some of them adopt performance data available from catalogs, corrected to account for the coefficient of performance variation in off-design conditions [12],[20]. Others, on the contrary, put forth an experimental campaign to map the system's performance, without providing insights into the action of the embedded controls [11].

Finally, other papers performed detailed thermodynamic modeling of the systems, without any focus on the chillers' embedded controls [10].

Considering the interest of research in optimizing chillers' energy performance and in investigating their potential role in improving buildings' flexibility, the provision of modeling grounded on a detailed thermodynamic basis and architecture control is of paramount importance to achieve more reliable results. Indeed, the developed models should provide insights into (i) the ability of the systems to quickly respond to the variation in the cooling (or heating) demand of the users (e.g., buildings or cooling network); (ii) the capability to adapt to the variation in the electricity produced by local RES while accounting for limits of the electric motor and the embedded controller, and (iii) the possibility to compare new control strategies aimed at improving the overall energy performance or to change operation according to ancillary services required by grid operators. Only a few papers have addressed some of these aspects [30]-[31]. For instance, Liu et al. [30] highlighted that when cooling systems are used for fast load balancing, the drastic changes in the compressor speed can cause severe superheat regulation issues including oscillations and even wet compression. Maier et al. [32] proposed a piecewise linear model based on simulation results and a quadratic modeling approach air-source heat pump while considering the supply temperature as a control variable. Both models were compared to a simplified linear model, which was found to underestimate operating costs. Clauß and Georges [31] investigated the influence of the modeling of the vapor compression systems control in the context of demand response. The authors compared different controls (e.g., proportional, continuous, etc.) and they demonstrated that the modeling complexity of the system control has a significant impact on the key performance indicators, proving that this aspect should not be overlooked. For instance, for short time operation, the modeling of the heat pump controller and the transient effects of the heat pump, such as cycling losses during start-up, are important.

To cover this knowledge gap, this paper proposes an integrated thermodynamic and control modeling of an air-cooled chiller. The thermodynamic modeling is first developed by relying on simulation data obtained using software where detailed analysis of heat exchanger and compressor operation is performed [33]. Regarding the induction motor, a full-scale state-space model is built, and the implementation of a variable speed drive is also carried out. Two architecture controls aimed at modulating the delivered cooling capacity are also presented. All the developed models are then jointly solved by using MATLAB Simulink [34]. By using the proposed model, the following aspects could be addressed:

- the comparison of different strategies for modulating the capacity delivered by chillers, while considering constraints related to the motors and controller. In this case, the following strategies for compressor management are analyzed: (i) a sequential control of multiple compressors, which consists of switching "ON" and "OFF" each compressor in the case of changes in user demand; and (ii) a variable-speed control which continuously varies the rotating speed of the compressors, allowing then for a smooth variation in the delivered cooling capacity.

- the analysis of the effect of the design of the hydronic circuit on the chiller's dynamic response (e.g., the average time needed by the unit to achieve the steady-state operation) and average energy performance.
- the provision of a model for simulating the operation of the chillers in the case of new management strategies aimed at increasing energy savings or building flexibility. In this respect, this paper proposes a supervisory control of the chillers which assumes a variable temperature setpoint of the produced cold water with the outdoor temperature, aimed at increasing energy efficiency and providing ancillary service to the grid.

To show the capabilities of the proposed model, an air-cooled chiller serving an office located in Southern Italy is assumed as the case study. Some scenarios will be simulated to account for the control strategies adopted and the effects of hydronic loop inertia. The paper is structured as follows: in the second section, details on the thermodynamic, electromechanical, and control modeling are provided. In the third section, the case study is described together with the simulated scenarios. In the fourth section, results will be presented and discussed, and in the final section, conclusions are briefly drawn.

2. Materials and Method

In this section, the modeling of an air-cooled chiller and the electric motors are presented. Then, a description of the control architecture together with details on implementation is provided.

2.1 Thermodynamic modeling of air-cooled chillers

Figure 1 shows a simplified schematic of an air-cooled chiller to depict the main subcomponents, physical variables, and acronyms widely used in the following. The major components are (i) an air-to-refrigerant heat exchanger (e.g., a tube and fins coil or plate and fins) used as the condenser (CND); (ii) a brazed-plate heat exchanger used as the evaporator (EVP) where water coming from the hydraulic loop at a temperature T_{wr} is cooled down to T_{ws} (iii) an expansion valve (EV); (iv) a compressor (CMP) coupled with an induction motor (IM). As will be explained later, to maintain a desired value of the temperature of the water supplied to the hydronic circuit (T_{ws}), the main controller (CTRL) will act on the electrical motor by regulating the rotating speed of the CMP or cycling it "ON" and "OFF".

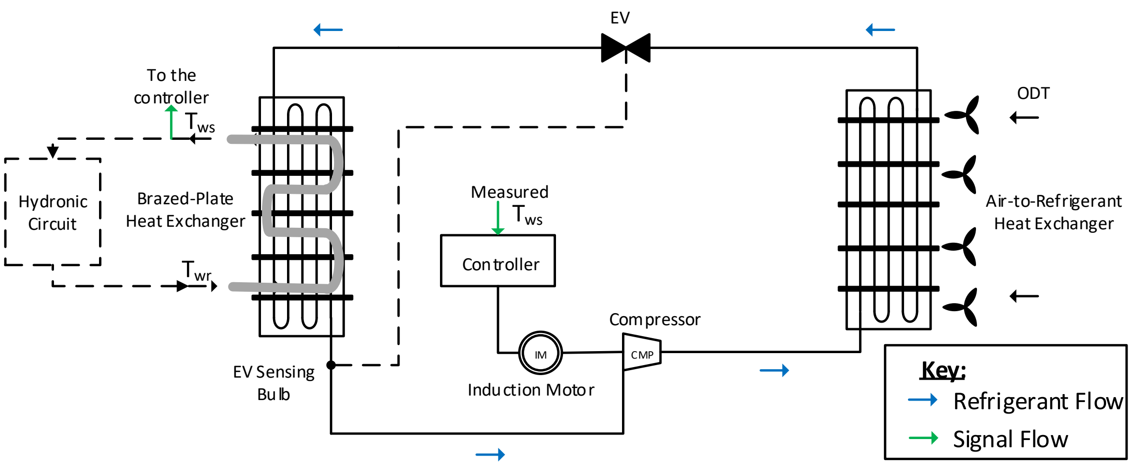

Figure 1. Simplified scheme of an air-cooled chiller.

The cooling capacity delivered (*CC*) and the mechanical power required by the CMPs (P_{m}) are necessary for assessing the energy performance of the chiller. Typically, the CMP rotating speed (ω_{CMP}), the dry-bulb temperature of the outdoor air (*ODT*), and the temperature of the water returning from the hydronic circuit and entering the evaporator (T_{wr}) are the variables that mostly influence the system performance, at given design and refrigerant charge [35]. It is then useful to develop ad-hoc equations like the ones shown in Eqs 1.a-b, where *CC* and P_{m} can be directly calculated in any operating conditions from the selected independent variables (typically available from measurement).

$$CC = f\ (\omega_{\mathrm{CMP}}, ODT, T_{\mathrm{wr}}\ ) \tag{1.a}$$

$$P_m = g(\omega_{\mathrm{CMP}}, ODT, T_{\mathrm{wr}}\ ) \tag{1.b}$$

However, to develop Eqs 1.a-b, a preliminary mapping of chiller behavior in a wide range of operating conditions is due. To this purpose, as it will be shown in Subsection 3.1, ad-hoc experimental campaigns or accurate plant simulations have to be performed. In this paper, Eqs 1.a-b are then formulated as shown in Eqs 2.a-b (more details about the accuracy of this assumption are provided in Subsection 3.1).

$$CC = L_1\omega_{\mathrm{CMP}} + L_2 ODT + L_3 T_{\mathrm{wr}} \tag{2.a}$$

$$P_m = K_1\omega_{\mathrm{CMP}} + K_2 ODT + K_3 T_{\mathrm{wr}} \tag{2.b}$$

In Eqs 2.a-b, K_{i} and L_{i} are fitting coefficients that can be found by applying numerical methods to the developed dataset.

The temperature of the water entering the EVP, i.e., T_{wr}, is obtained from the dynamic model of the hydronic circuit served by the chiller. This simplified model [36], sufficiently reliable for the scope of this paper, is presented in Eq. 3,

$$\frac{dT_{\mathrm{wr}}}{dt} = \frac{1}{C_{\mathrm{s}}}(CL - CC) \tag{3}$$

where the time variation of T_{wr} is proportional to the difference between the building cooling load (i.e., CL) and CC. C_s is a coefficient (measured in kJ/°C) that quantifies the thermal inertia of the hydronic loop coupled to the chiller. This parameter is highly dependent on the water content in the hydronic circuit, and its value is usually determined during the design phase of the circuit to assure the safe operation of the CMPs of the cooling systems. Eqs 4.a-b are used to estimate this quantity. In particular, Eq. 4.b is also known as the "Portoso's Equation" [37] which is typically used in Italy during the design phase of hydronic loops served by chillers [3].

$$C_s = \rho_{\mathrm{w}}\, c_{\mathrm{w}} V_{\mathrm{des}} \tag{4.a}$$

$$V_{\mathrm{des}} = \frac{60 CC_{\mathrm{nom}}}{\rho_{\mathrm{w}}\, c_{\mathrm{w}} \left(\frac{\Delta T_{\mathrm{wr}}}{\Delta \tau}\right)_{\mathrm{ref}}} \tag{4.b}$$

In Eqs 4.a-b ρ_{w} is the density of water, c_w is the specific heat capacity of water, and V_{des} is the volume of water in the hydronic loop, which should be sufficient to guarantee the safe operation of the chiller. CC_{nom} is the nominal cooling capacity delivered by the chiller at the design condition and $\left(\frac{\Delta T}{\Delta \tau}\right)_{\mathrm{ref}}$ is the maximum variation of the water return temperature from the hydronic loop in one minute. Typically, it is assumed to be equal to 5 °C/min [37]. This value was derived from observation in the field. The temperature of the water supplied to the building (T_{ws}) is simply computed by the energy balance shown in Eq. 5,

$$T_{\mathrm{ws}} = T_{\mathrm{wr}} - \frac{CC}{\dot{m}_{\mathrm{w}} c_{\mathrm{w}}} \tag{5}$$

where $\dot{m}_w$ is the mass flow rate of water circulating in the hydronic loop. The mass flow rate of water is constant throughout the operational period. Worth noting that T_{ws} is typically assumed as the controlled variable by the controller.

The mechanical load torque T_{L} required by the CMP is then calculated using Eq. 6, where the factor $\frac{60}{2\pi}$ is used to covert the CMP rotating speed (ω_{CMP}) from rpm/min to rad/s.

$$T_{\mathrm{L}} = \frac{60\ P_m}{2\pi\ \omega_{\mathrm{CMP}}} \tag{6}$$

2.2 State-space model of the induction motor

An IM is used to supply mechanical power to CMP. To model the dynamic response of the IM, a 5th-order linear state-space model in the stationary reference frame is adopted as detailed in Eq. 7 [38,39]:

$$\frac{d}{dt}\begin{bmatrix} i_{\mathrm{s}} \\ \varphi_{\mathrm{r}}' \end{bmatrix} = \mathrm{A}\begin{bmatrix} i_{\mathrm{s}} \\ \varphi_{\mathrm{r}}' \end{bmatrix} + \mathrm{B}\, u_{\mathrm{s}} = \begin{bmatrix} A_{11} & A_{12} \\ A_{21} & A_{22} \end{bmatrix}\begin{bmatrix} i_{\mathrm{s}} \\ \varphi_{\mathrm{r}}' \end{bmatrix} + \begin{bmatrix} B_1 \\ B_2 \end{bmatrix} u_{\mathrm{s}} \tag{7}$$

In Eq. 7, $\begin{bmatrix} i_{\mathrm{s}} \\ \varphi_{\mathrm{r}}' \end{bmatrix}$ is the vector of state variables, i.e., i_{s} and φ_{r}'. In addition, i_{s} are the stator currents (i_{sq} and i_{sd}) and φ_{r}' are the rotor fluxes in direct and quadrature axis (φ_{rd}' and φ_{rq}'). Both vectors are referred the stationary reference frame of the machine. "A" is a 4x4 compound matrix filled with the coefficients of the state variables which are summarized in Table 1. u_{s} is the vector of stator voltages in direct and quadrature axis, indicated as u_{sq} and u_{sd} respectively. The B vector has the coefficient of the input variable of the stator voltage u_{s}, and the elements of this vector are presented in Table 1 as well.

Table 1. Elements of A and B matrices for the IM state-space model.

$A_{11} = -\left(\frac{R_{\mathrm{s}}}{\sigma L_{\mathrm{s}}} + \frac{1-\sigma}{\sigma T_{\mathrm{r}}}\right) I$	(7.a)	$B_1 = \frac{1}{(\sigma L_{\mathrm{s}})} I\,, B_2 = \begin{bmatrix} 0 & 0 \\ 0 & 0 \end{bmatrix}$	(7.e)
$A_{22} = -\frac{1}{T_{\mathrm{r}}} I - \omega_{\mathrm{r}} D$	(7.b)	$C = [I \quad 0]$	(7.f)
$A_{12} = \frac{L_{\mathrm{m}}}{\sigma L_{\mathrm{s}} L_{\mathrm{r}}}\left(\frac{1}{T_{\mathrm{r}}} I - \omega_{\mathrm{r}} D\right)$	(7.c)	$I = \begin{bmatrix} 1 & 0 \\ 0 & 1 \end{bmatrix}$	(7.g)
$A_{21} = -\frac{1}{\sigma L_{\mathrm{s}}} I$	(7.d)	$D = \begin{bmatrix} 0 & -1 \\ 1 & 0 \end{bmatrix}$	(7.h)

In Table 1, R_{s} is the stator resistance, L_{s} is the stator inductance, T_{r} the rotor time constant, L_{r} is the rotor inductance, L_{m} is the mutual inductance, σ is equal to $(1 - \frac{{L_{\mathrm{m}}}^2}{L_{\mathrm{s}} L_{\mathrm{r}}})$. C, I and, D are matrices used to present the equations in the direct and quadrature axis.

From the states obtained by solving Eq. 7, the electromagnetic torque of the IM, i.e., T_{el} is then evaluated by using Eq. 8, where p is the number of pair poles. Mechanical dynamic is then presented in Eq. 9, where the resulting output is the mechanical speed or also referred to as the CMP speed ω_{CMP}. Note that, the mechanical torque required by the chiller, which was previously indicated as T_{L}, is given by Eq. 6, where J is the inertia of the rotor and μ is the viscosity friction of the rotor.

$$T_{\mathrm{el}} = 1.5p(i_{\mathrm{sq}}\, \varphi_{\mathrm{rd}}' - i_{\mathrm{sd}}\, \varphi_{\mathrm{rq}}') \tag{8}$$

$$J\frac{d\omega_{\mathrm{CMP}}}{dt} + \mu\, \omega_{\mathrm{CMP}} = T_{\mathrm{el}} - T_{\mathrm{L}} \tag{9}$$

2.3 Description and modeling of the chiller's control architecture

Air-cooled chillers could be equipped with constant-speed or with variable-speed CMPs. From a survey of several commercial catalogs, chillers with a nominal cooling capacity of less than 60 kW_c are typically equipped with CMPs with a variable speed drive (VFD), and the CMP rotating speed is varied to meet a desired supply water temperature setpoint ($T_{ws,ref}$). Conversely, for larger units, multiple constant-speed CMPs are used, and an "ON-OFF" control strategy is followed to vary the delivered capacity according to some signal from local thermostats. In the next subsections, a description of the control architectures is provided together with details on the modeling.

2.3.1 Control architecture for variable-speed air-cooled chillers

In Figure 2, the control architecture for a variable-speed air-cooled chiller is shown. In this case, the CMP rotating speed (provided by the IM) is modulated through the action of the VFD (indicated by the grey-dotted box). A scaler control is used inside the VFD. The main reason for implementing scalar control over other advanced control methods such as Field-Oriented Control or Direct-Torque Control is the simplicity of implementing the control technique in software and hardware. As a result, the overall cost is also minimized since the controller can be realized using a low-cost microprocessor. Secondly, the reason to deploy advanced control methods is that scalar control operation is poor at low speeds. For this application, the IM is operational only at high speeds, and the usage is justified. The scaler control uses a simple "voltage over frequency V/F" technique to control an IM at variable speeds. More details on scaler control are provided in [39]. As shown in Fig. 2, a proportional and integral (PI) temperature controller provides a reference value of speed for the V/F control (i.e., ω_{ref}) based on the difference between the measured supply water temperature and the desired value (i.e., ΔT_{ws}). Then, based on ω_{ref} value, the V/F control provides the duty cycles, $D_{a,b,c}$ for each of the inverter switching devices. Space vector modulation (SVM) is used to acquire the duty cycles for each of the inverter switching devices. Finally, the Voltage Source Inverter (VSI) provides the three-phase voltage $V_{a,b,c}$ input to the IM.

In the "air-cooled chiller" block, the thermodynamic model of the chiller (see subsection 2.1) is implemented. The overall architecture can be solved in software, such as MATLAB Simulink.

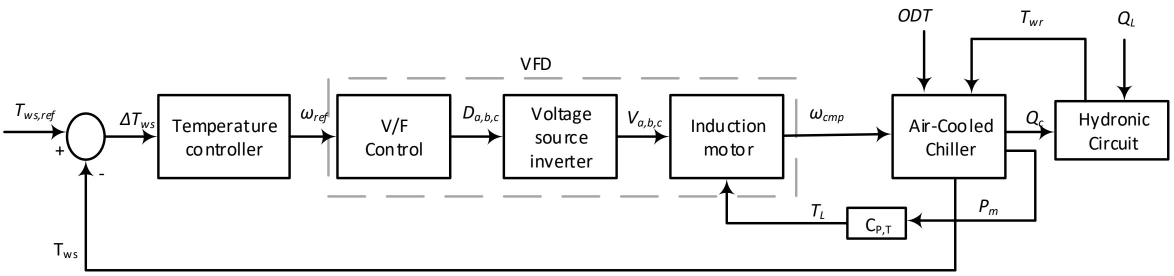

Figure 2. Architecture control for a variable-speed air-cooled chiller.

2.3.2 Control architecture for constant-speed chillers with multiple compressors

A control approach frequently used to modulate the delivered capacity of chillers is to cycle CMPs "ON-OFF" to maintain the water supply temperature (T_{ws}) around a desired value, as shown in Figure 3. In this case, CMP rotating speed has a unique nominal value, and it is not modulated as in the case of VFD. If more than one CMP is available, that is a very common practice to guarantee more flexible modulation of cooling capacity, a logic must be used to coordinate the "ON-OFF" cycle of each of them. Typically, a sequential approach (or sequential control SC) is adopted. For the sake of clarity, Figure 3 shows a typical SC in the case of a chiller equipped with two CMPs. The black line represents the measured value of the water supply temperature. The horizontal blue lines indicated by $T_{ws} \pm \Delta T_{ws,n}$ values represent the temperature threshold values for activating or deactivating each CMP. Low values for $\pm\Delta T_{ws,n}$ could lead to many "ON-OFF" cycles of each CMPs. Conversely, large values could lead to high T_{ws} fluctuations. Hence, the values of $\pm\Delta T_{ws,n}$ are selected to assure a maximum number of "ON-OFF" cycles in an hour, thus increasing the CMPs' lifetime.

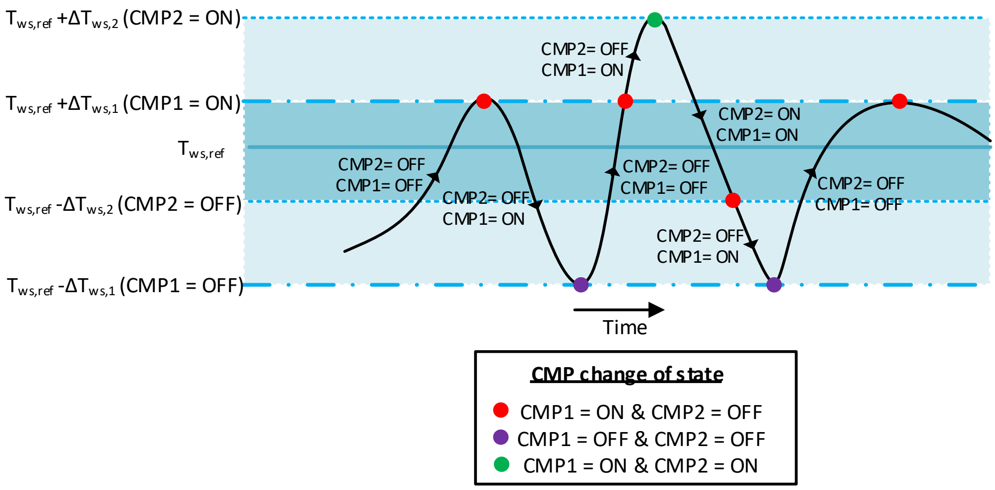

Figure 3. Sequential control for an air-cooled chiller equipped with two constant-speed CMPs.

Figure 4 presents the architecture scheme for sequential control. A simple hysteresis controller can be used to implement the “ON-OFF” sequence of each CMP, which is assigned to work in a range of $\pm\Delta T_{\mathrm{ws,n}}$. Worth noting that the hysteresis controller for each CMP can be simulated by using the built-in block named “hysteresis comparator” available in MATLAB Simulink.

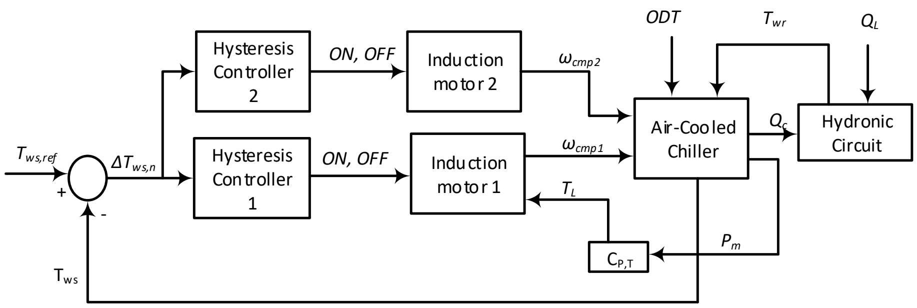

Figure 4. Architecture control for the sequential control strategy.

3. Case study: description, modeling, and simulation

An office building located in Palermo (Italy) is selected as a case study. Demand profiles are estimated using data available from energy audits performed in a previous study [40]. Two working days in the cooling period are here examined. One is characterized by a high cooling demand (i.e., around the end of July), and the other one by a low demand (i.e., around the half of June). In Figure 5.a-b, the values of *ODT* and cooling load are presented. Worth noting that, the dashed line is used for the profile in the low-cooling load day and the continuous line for the high-cooling load day. Focusing on the building load, it is assumed an operation for 9 hours during a day, (from 8 am to 5 pm) with a variation of the load at 15 minutes. In addition, as shown in Figure 5.a, the *ODT* values vary on an hourly basis, and the values are retrieved from a meteorological dataset [41].

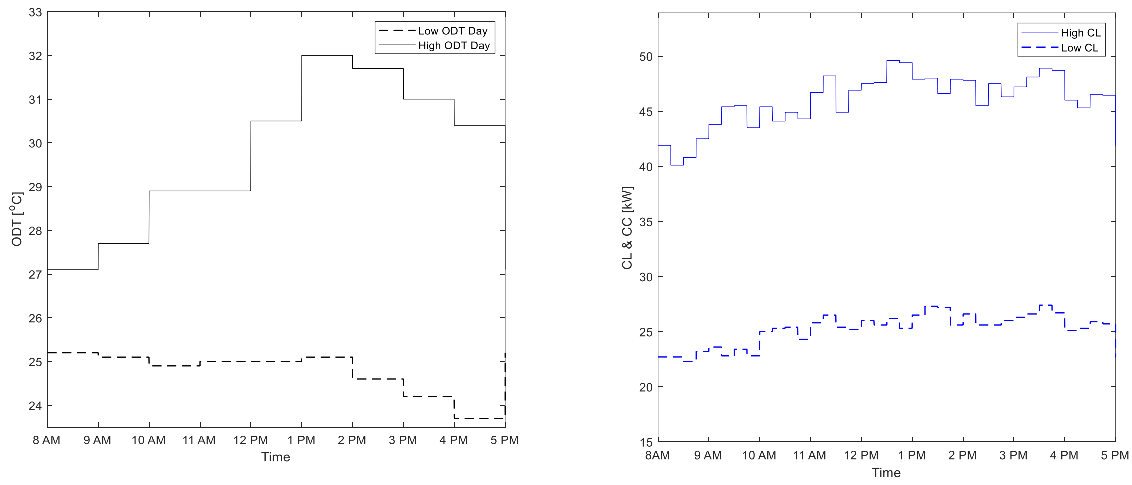

(a) (b)

Figure 5. Daily profiles of low- and high-cooling load days: (a) *ODT* values, (b) cooling demand.

The nominal capacity of the chiller was selected based on the peak value of the cooling demand, equal to around 50 kW$_c$. In Table 2, the technical data of the refrigerant circuit and IM are shown. Note that these data are derived from commercial catalogs.

Table 2. Technical details on a 50 kW$_c$ air-cooled chiller and electrical parameters of the induction motor.

Refrigerant Circuit		**Induction Motor**	
Refrigerant	R410a	P_n(kW)	10
CND Type	Fin and Tube	R_s (Ω)	0.8
Number of CND	1	R_r(Ω)	2.91
CND Fan Power [kW]	1.5	L_s(H)	0.21
Metering Device	Electronic Expansion Valve (EEV)	L_r(H)	0.21
EVP Water Flowrate [m^3/h]	7.0	L_m(H)	0.2
EVP Pump Power [kW]	2	J(kg.m^2)	0.1
CMP Type (and Number)	Scroll (2)	σ (-)	0.03
CMP Power (each) [kW]	9.0	f(Hz)	50
Refrigerant Charge [kg]	14.3	p	2

As shown in Table 2, the chiller is equipped with two scroll CMPs. For the scope of this paper, two control strategies for CMPs are considered:

- *variable-speed CMP* (in the following indicated also as a variable-speed chiller) according to which the speed of both CMPs is continuously varied between a minimum and a maximum value by the VFDs. From a survey of commercially available scroll CMPs, the rotating speed ω_{CMP} is assumed to vary between 1000 and 6200 rpm.
- *"ON-OFF" CMPs* with sequential control (in the following briefly indicated as a constant-speed chiller) according to which CMPs speed is kept constant (typically, 2900 rpm) once switched ON, and the cooling load is satisfied by cycling "ON-OFF" the CMPs according to the sequential approach shown in Fig. 3.

3.1 Details on the performed simulations

The thermodynamic models of the air-cooled chillers are developed by using the IMST-Art software [33]. The tool implements 1-D thermohydraulic modeling of heat exchangers, refrigerant lines, and accessories, and its reliability has been proven by accurate validation against wide sets of experimental results [42]. To map the chiller's performance, different simulations are developed for both variable-speed and constant-speed chillers, based on the matrix test shown in Table 3. As can be observed, *ODT* is varied over a wide range (from 22 up to 38 °C) to account for possible application of the same model in different climatic conditions. A step variation equal to "+2 °C" is assumed, leading to nine values to be simulated. Regarding the temperature of the water returning from the hydronic circuit, T_{wr}, the range 8-14 °C is selected to account for different heating/cooling demands. For this variable, a variation step of "+2 °C" is assumed as well, leading to four T_{wr} values to be simulated.

In the case of the variable-speed chiller, the rotating speed of each CMP is varied (both operating simultaneously) between 1000 and 6200 rpm, with a step equal to "+400 rpm" and fourteen ω_{CMP} values had to be simulated). The number of simulation tests to be performed in IMST-Art is then obtained by combining nine *ODT* values, four T_{wr} values, and fourteen CMP speeds.

Regarding the constant-speed chiller, as shown in Table 3, the rotating speed of each CMP was set to 2900 rpm, as suggested by a commercial catalog [43]. Simulations are first performed by combining the nine *ODT* values and the four T_{wr} values and considering that only one CMP is operating. Then, the tests are repeated considering both CMPs activated.

Table 3. Matrix test for the air-cooled chiller thermodynamic modeling.

		Range	**Change Step**	**Variable-Speed Chiller**		**Constant-Speed Chiller**			
				ω_{CMP} [rpm]		ω_{CMP1} [rpm]		ω_{CMP2} [rpm]	
ODT	[°C]	22-38	+2 °C	Range	Change Step	"ON"	2900	"ON"	2900
$T_{w,r}$	[°C]	8-14	+2 °C	1000-6200	(+400 rpm)	"OFF"	0	"OFF"	0

The linear coefficients of Eqs 2.a-b are obtained by using the Least-Square technique. In Table 4, the coefficients for the mechanical power and delivered capacity are shown for the variable-speed chiller. In Table 5, the results for the constant-speed chiller are detailed. Worth noting that to evaluate the error index of the realized model in comparison to the thermodynamic data, the Normalized Root Mean Square Error Index (NRMSE) is here used. Since the NRMSE values in Tables 4 and 5 are always less than 5%, a good approximation of simulation data is achieved by the proposed model.

Table 4. Values of the fitting coefficients for the variable-speed chiller.

	Delivered Capacity			**Absorbed Power**		
VS-Cooling	L_1	0.009	RMSE [kW]:	K_1	0.004	RMSE [kW]:
	L_2	-0.32	2.26	K_2	0.05	1.41
	L_3	1.55	NRMSE [%]: 3.91	K_3	-0.26	NRMSE [%]: 5.91

Table 5. Values of the fitting coefficients for the constant-speed chiller.

	Delivered Capacity One CMP-ON			Absorbed Power One CMP- ON		
CS-Cooling	L_1	0.012	RMSE [kW]:	K_1	0.0008	RMSE [kW]:
	L_2	-0.38	0.15	K_2	0.16	0.03
	L_3	0.97	NRMSE [%]: 1.15	K_3	0.018	NRMSE [%]: 0.98
	Delivered Capacity Two CMPs-ON			**Absorbed Power Two CMPs- ON**		
	L_1	0.02	RMSE [kW]:	K_1	0.002	RMSE [kW]:
	L_2	-0.6	0.24	K_2	0.38	0.07
	L_3	1.58	NRMSE [%]: 1.87	K_3	0.043	NRMSE [%]: 2.33

3.2 Implementation of the integrated control scheme and main assumptions for the analysis

The overall schemes for sequential control and variable speed are implemented in MATLAB Simulink. Since the simulation considers the full-day operation, a sample time equal to 0.01 s (quite large, compared to the typical values adopted for VFDs' modeling) is used to reduce the data point. The variable-speed chiller is controlled by assuming a 7 °C setpoint value for the supply water temperature. The tuning of the PI parameters in the Temperature Controller (see Fig. 2) is performed via MATLAB *Sisotool* command [34]. By fixing a settling time of 10 minutes, the command provides the values of the proportional and integral gains to the users.

Regarding the constant-speed chiller with sequential control, a 7 °C value for the $T_{\mathrm{ws,\,ref}}$ is assumed. However, as previously explained (see Figure 3), appropriate temperature bands are required to avoid too many cycles of CMPs. For this case, the selected temperature bands are detailed in Table 6.

Table 6. Bands definitions for CMPs cycling in sequential control.

Changes in CMP State	Threshold values
CMP 1: ON, **CMP 2:** ON	$T_{ws\,,CMP2\_ON} = 8.0\ °C$ (ΔT_{ws}= +1.0 °C)
CMP 1: ON, **CMP 2:** OFF	$T_{ws\,,CMP1\_ON} = 7.5\ °C$ (ΔT_{ws}= +0.5 °C)
CMP 1: ON, **CMP 2:** OFF	$T_{ws\,,CMP2\_OFF} = 6.5\ °\mathrm{C}$ ($\Delta T_{\mathrm{ws}} = -0.5\ °\mathrm{C}$)
CMP 1: OFF, **CMP 2:** OFF	$T_{ws\,,CMP1\_OFF} = 6.0\ °\mathrm{C}$ ($\Delta T_{\mathrm{ws}} = -1.0\ °\mathrm{C}$)

To evaluate the energy performance achieved by different control strategies of the chiller, the Energy Efficiency Ratio (*EER*) averaged on an hourly basis is used and defined in Eq. 10.

$$EER = \frac{\int_0^{3600} CL(t)dt}{\int_0^{3600} P_e\,(t)dt} \tag{10}$$

3.3 Variable water-supply-temperature control strategy

As previously mentioned, it is of utmost importance to develop chillers' modeling for simulating new control strategies aimed at (i) increasing the *EER* of the chiller or (ii) providing ancillary services to the grid under the current scenarios of growing interest for smart grids, where an active role in grid-balancing is often played by customers.

In this paper, the possibility to operate a chiller with a sliding $T_{ws,ref}$ is investigated. Worth noting that $T_{ws,ref}$ is usually set to 7 °C regardless of the *ODT* value. The use of sliding water supply temperatures (variable with the *ODT*) is very common in hydronic heating but rarely adopted in space cooling despite its significant energy-saving potential. Indeed, the possibility for the chiller to operate with higher evaporation pressures during moderately warm periods could lead to higher *EER* values. The reason for this scarce use of sliding water supply temperatures in hydronic cooling lies in the risk to lose control of indoor relative humidity. Depending on the type of equipment supplied (*e.g.*, fan coils, cooling coils in air handling units, etc.) the water inlet temperature is a key parameter to guarantee the required moisture removal from the treated air. Then, a preliminary assessment of the effects of chilled water supply temperature on the dehumidification capacity of coils is developed, based on the model proposed by Braun [44]. A cooling coil consisting of three rows, and eight tubes per row (typical configuration for commercial fan coils) is assumed as a reference. The analysis is aimed at assessing the changes in the Sensible Heat Ratio (*SHR*) of the coil when it is supplied by chilled water at different temperatures but with a constant flow rate. The results are shown in Fig. 6, with the cooling capacity and the *SHR* plotted vs. the chilled water temperature at the coil inlet. The resulting trends are also validated against data from catalogs of commercial fan-coil systems [45]. The T_{ws} varies in the range of 7.0-12.0 °C and significant reductions in both the sensible and latent capacity at higher water temperatures are observed. However, since the latent capacity of the coil for T_{ws} values above 10 °C is almost less than 50% compared to the value found at 7 °C, it is preferable to limit the supplied water temperature fluctuations to the 7.0-9.5 °C range (also indicated by the area in Fig. 6 not covered by the light blue rectangle) so that the dehumidification capacity of the coil is only moderately affected. In quantitative terms, when T_{ws} increases from 7.0 to 9.5 °C, the sensible cooling capacity slightly decreases from 2.86 down to 2.55 kW (-10.8%) while the latent capacity decreases from 1.04 kW down to 0.81 kW (-22.12%). Consequently, the *SHR* passes from 0.73 at 7 °C up to 0.8 at 9.5 °C, with a moderate 8.75% increase that sounds acceptable for most space cooling applications, whenever very strict control of indoor relative humidity is not required.

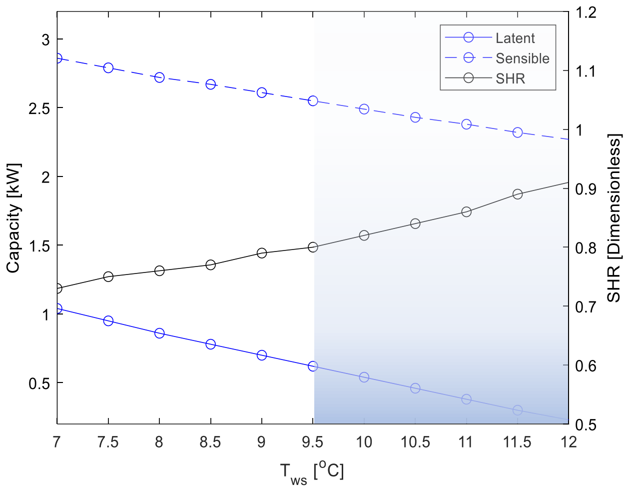

Figure 6. Sensitivity of coil capacity and SHR to the inlet temperature of chilled water.

Based on the above results, the assumption of a sliding supply temperature of chilled water over the 7.0-9.5 °C range sounds technically feasible. Then, it is worth investigating the variation in the performance of the chiller under such conditions to assess the potential benefits in terms of energy savings. As shown in Fig. 7, a linear change in $T_{ws,ref}$ is assumed. In particular, $T_{ws,ref}$ is maintained at 7 °C for *ODT* values higher than 30 °C. A linear increase from 7 °C up to 9.5 °C is assumed when *ODT* gradually decreases from 30 °C down to 24 °C. For *ODT* values lower than 24 °C , $T_{ws,ref}$ is set to 9.5 °C.

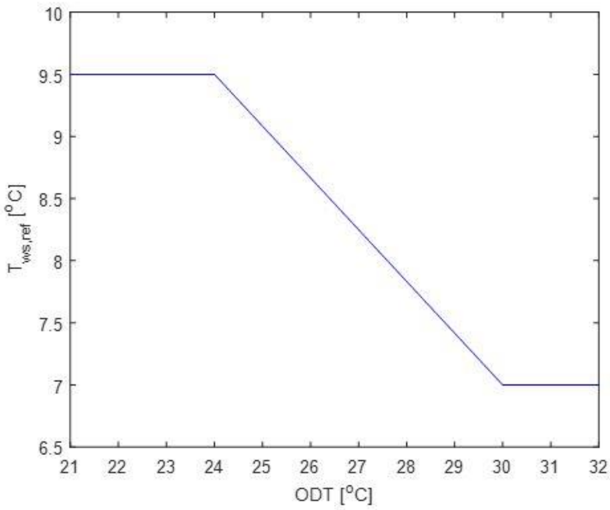

Figure 7. Variable set-point for the supply temperature of chilled water vs. *ODT*.

4. Results and Discussion

Simulation results for the variable-speed and constant-speed chiller are first shown. Results from the sensitivity analysis are then discussed. In the last subsection, results for the flexible operation of the chiller are presented.

4.1 Variable-speed air-cooled chiller

Figures 8.a-e show results for the variable-speed chiller operation on the high cooling load day. Note that, for the sake of brevity, in this case, only results for the high cooling load day are shown. However, similar considerations could be made for the low cooling day. In Fig. 8.a, the delivered *CC* (blue dashed line) is presented along with the *CL* profile (blue continuous line). Looking at the *CC* profile, it is worth noting that the chiller is constantly trying to match the cooling load. As it can be observed from the zooming at 11-12 am in Figure 8.a, the cooling capacity has an oscillating trend at each change in the load due to the action of the PI controller. Figure 8.b shows the temperature of the water supplied to the building. Worth noting that T_{ws} is maintained almost at 7 °C (the assumed setpoint) thanks to the controller. Some oscillations are present every 15 minutes due to the changes in *CL*. As shown in Fig. 8.b, the rotating speed of the CMPs is continuously manipulated to meet the water supply temperature setpoint. In Fig. 8.c, both the electromagnetic torque produced by the IM and the CMP torque are plotted. Since both curves are perfectly overlapped, it follows that a dynamic equilibrium is achieved between the CMP and the IM during the operation. Fig. 8.d shows the sum of the mechanical power supplied by both the IMs to the CMP. In Fig. 8.e, the absorbed RMS current by the IMs is plotted. Minimal fluctuations in the root mean square value of currents are observed. As a result, the measured value is always close to 8.2 A. The initial spike accounts for the inrush current to magnetize the IM. Fig. 8.f shows the average *EER* values calculated according to Eq. 10. The *EER* ranges between 3.43 and 3.08 during the operation due to the combined effect of part-load operation and *ODT* values.

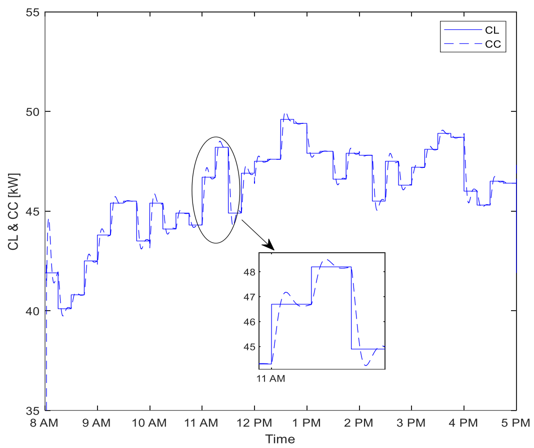

(a)

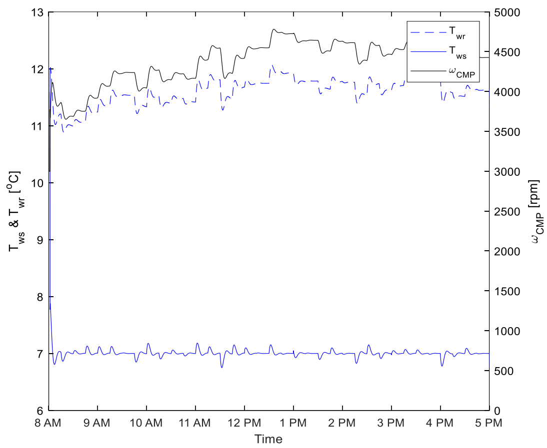

(b)

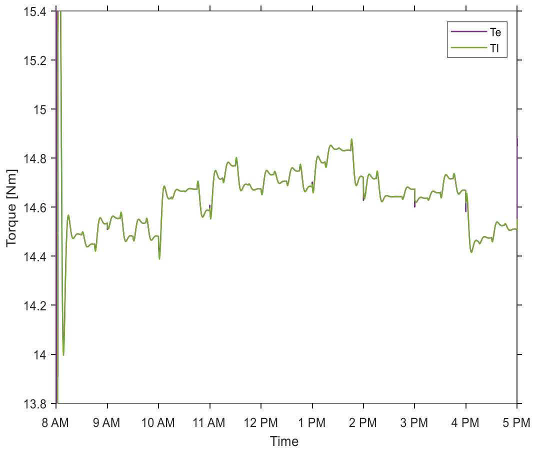

(c)

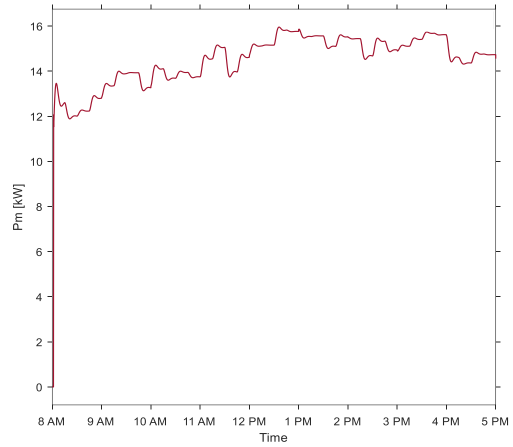

(d)

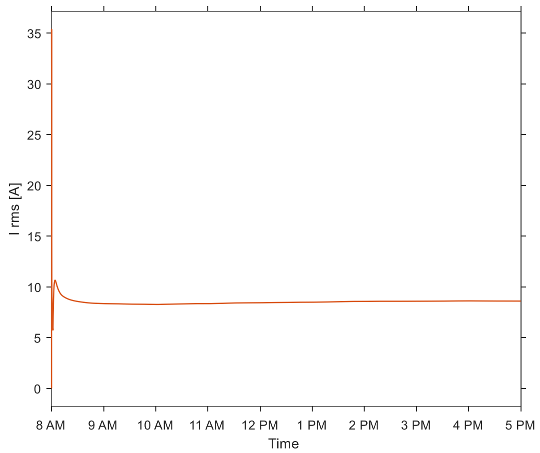

(e)

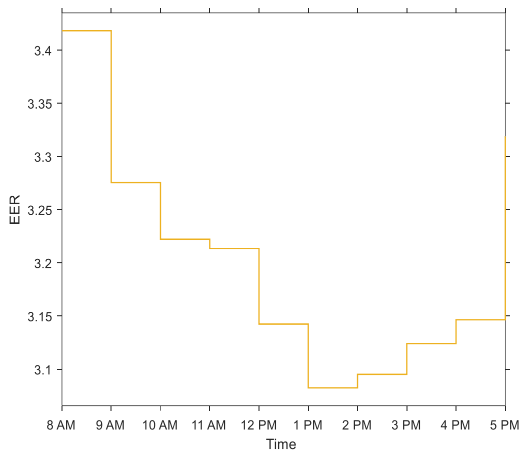

(f)

Figure 8. Variable-speed results: (a) Cooling Load and Cooling Capacity (b) Water supply temperature, Water return temperature, and CMP speed, (c) Mechanic and electromagnetic torque, (d) Mechanical Power, (e) Absorbed Current, (f) *EER*.

4.2 Constant-speed air-cooled chiller

Figures 9.a-d show the results for a constant-speed air-cooled chiller for the high cooling load day in Palermo. In Fig. 9.a the cooling demand profile (blue continuous line) is shown together with the capacity delivered by the chiller. The different pattern in the *CC* observed here compared to Fig 8.a is simply explained considering that CMPs are here cycled “ON-OFF”, thus leading to a discontinuous *CC* profile. Moreover, the minimum *CC* is never zero, since one CMP (i.e., CMP 1) is always operating. In this respect, as shown in Fig 9.b, the value of ω_{CMP1} is always 2900 rpm (red line), conversely ω_{CMP2} changes from 0 or 2900 rpm, according to the cycling (black line). Moreover, the temperature of the water supplied to the building is oscillating around the value of 7.25 °C value (black dashed line). In Fig. 9.c-d a zoom on two hours in the high cooling load day is shown. Fig. 9.c plots the CMPs’ operation from 8 to 9 am, when the lowest cooling demand is observed. Fig. 9.d focus from 11 to 12 am. CMP 1 is always operating, since on this day the minimum cooling load value (which is observed from 8 am to 9 am) is higher than the minimum capacity provided by the chiller with only one CMP operating. Conversely, CMP 2 is continuously cycling “ON-OFF” to match the load. As shown within the box in Fig. 9.c, from 8 to 9 am CMP2 is cycling “ON-OFF” almost 17 times, which is higher than the maximum threshold value equal to “12 cycles per hour” suggested by the manufacturer. From 11 to 12 am, instead, CMP 2 is cycling 19 times. In Figure 9.e, the mechanical power required by the CMPs is plotted. As expected, it is never equal to zero since CMP 1 is always ON. Fig. 9.f shows the average hourly *EER* values. The *EER* ranges between 3.29 and 2.85 during the operation due to the combined effect of part-load operation and different *ODT* values.

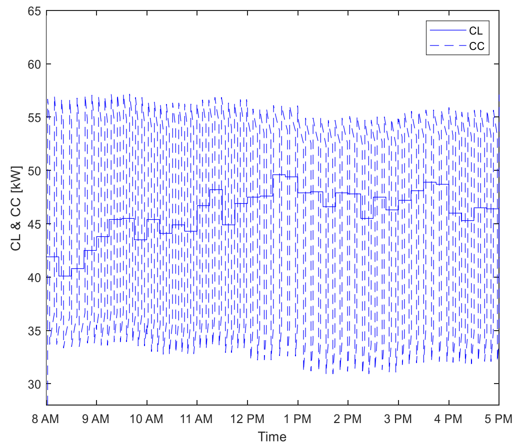

(a)

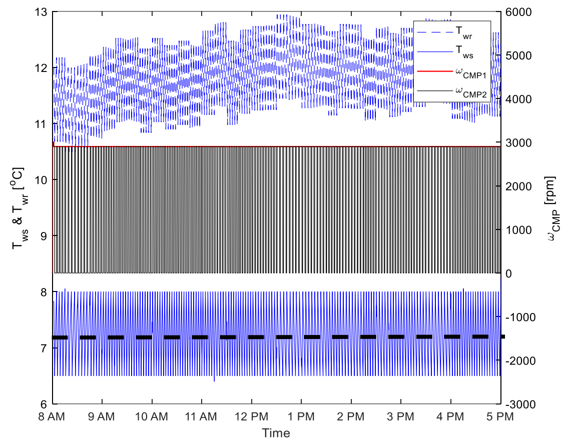

(b)

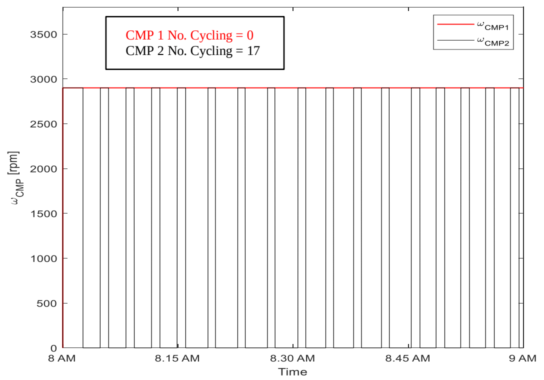

(c)

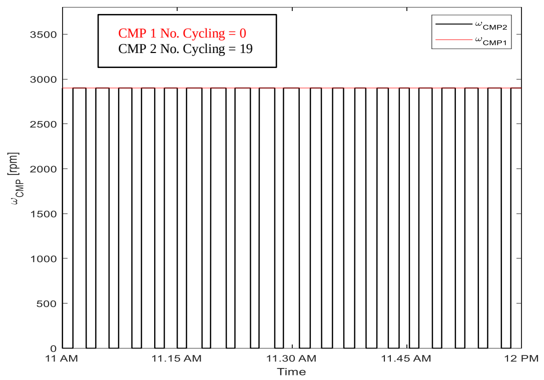

(d)

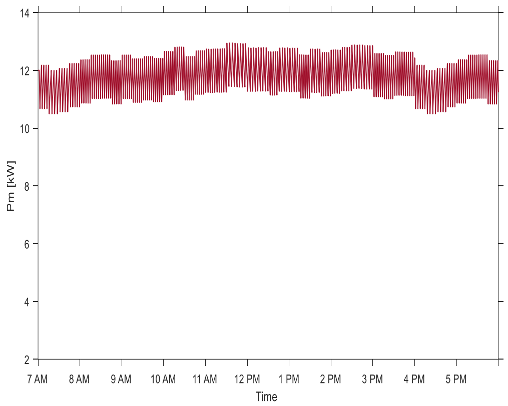

(e)

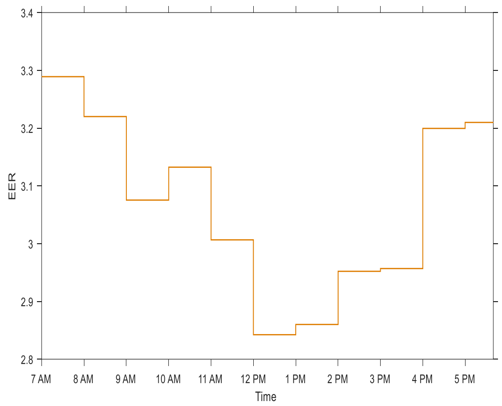

(f)

Figure 9. SC results for high-cooling load day: (a) Cooling Load and Cooling Capacity (b) Water supply, Water return temperature, and CMPs cycles, (c) CMPs' operation from 8-9 am, (d) CMPs' operation from 11-12 am, (e) Mechanical Power, and (f) *EER*.

Figures 10.a-d show the results obtained from simulations for a constant-speed air-cooled chiller on the low-cooling day in Palermo. As shown in Fig. 10.a, compared to Fig. 9.a, the minimum delivered CC is zero, meaning that the unit is completely OFF during the day. As shown in Fig 10.b, the value of ω_{CMP2} is always zero (black line), conversely, ω_{CMP1} changes from 0 to 2900 rpm, according to the cycling (red line). Moreover, the temperature of the water supplied to the building is oscillating around the value of 6.75 °C value (black dashed line). In Fig. 10-c-d a zoom on the low load (8-9 am) and high (11-12 am) hours of this day is shown. Fig. 10.c plots the CMPs' operation from 8 to 9 am. CMP 2 is ON only for some minutes at the very beginning of the selected hours due to the start-up of the plant. Then, CMP 2 is OFF for all the remaining working hours in the day, since the maximum cooling load value (observed from 1 to 2 pm) is lower than the minimum capacity provided by the chiller with two CMPs ON. Conversely, CMP1 is continuously cycling "ON-OFF" to match the cooling load. As shown in the box in Fig. 10.c, from 8 to 9 am CMP 1 is cycling "ON-OFF" almost 25 times, which is higher than the maximum threshold value equal to 12. From 11 to 12 am (Fig. 10.d), CMP 1 is cycling 21 times. In Figure 10.e the mechanical power required by the CMPs is plotted. As expected, its minimum value is zero in those moments where the unit is OFF. Fig. 10.f shows the average hourly *EER* values. The *EER* ranges between 2.96 and 3.27 during the operation due to the combined effect of part-load operation and different *ODT* values. These results highlight the importance of including detailed chiller modeling in studies focused on new control strategies for increasing energy savings or flexibility in those buildings equipped with chillers: indeed, in such cases, the risk of unsafe CMPs' operation can be easily predicted.

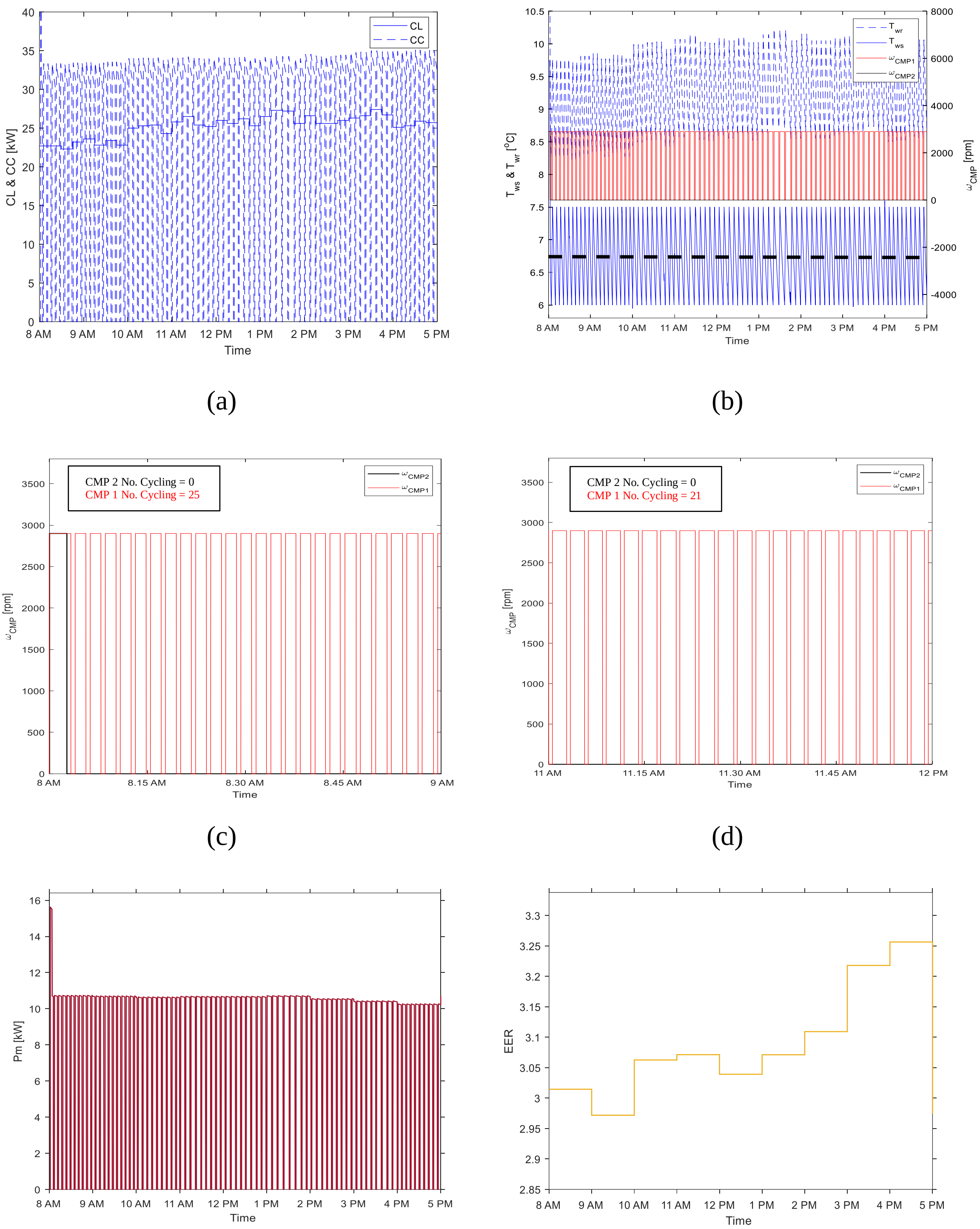

(a) (b) (c) (d) (e) (f)

Figure 10. SC results for low-cooling load day: (a) Cooling Load and Cooling Capacity (b) Water supply, Water return temperature, and CMPs cycles, (c) CMPs' operation from 8-9 am, (d) CMPs' operation from 11-12 am, (e) Mechanical Power, and (f) *EER.*

4.3 Sensitivity analysis with the design of the hydraulic loop

In the previous section, simulations were performed assuming a C_s equal to 600 kJ/°C. It is worth investigating the effect of different C_s values on the controller actions and overall energy performance. Then, simulations are performed considering the following C_s values: 500 -1000-1500 -2000 kJ/°C.

Results for the case of the variable-speed chiller are presented in Figure 11. In particular, Fig. 11.a-b presents the water supply temperature for all the C_s values at 8-9 am. Note that for the sake of clarity, only data for two hours, i.e., 8-9 am and 11-12 am are here presented for the high-cooling load (Fig. 11.a-b). In both figures, moving from the smallest value (i.e., 500 kJ/°C, blue line) to the highest one (i.e., 2000 kJ/°C, purple line), a reduction in the peak value of T_{ws} is observed after changes in the cooling demand. For instance, as shown in Fig. 5.a-b the temperature overshoot after a load change is almost halved passing from 500 kJ/°C to 2000 kJ/°C. Moreover, when increasing the C_s value, the oscillating behavior in T_{ws} is reduced, leading to a more stable chiller operation and the quick reaching of steady-state operation. Fig. 11.c presents the average hourly *EER* values. Worth noting that the variation of C_s has a negligible impact on hourly *EER* values. These results suggest that, in the case of variable-speed units, variation in the thermal inertia of the hydronic loop mainly affects the dynamic response of the chiller (overshoot of the supplied water temperature), while changes in energy performance are almost negligible.

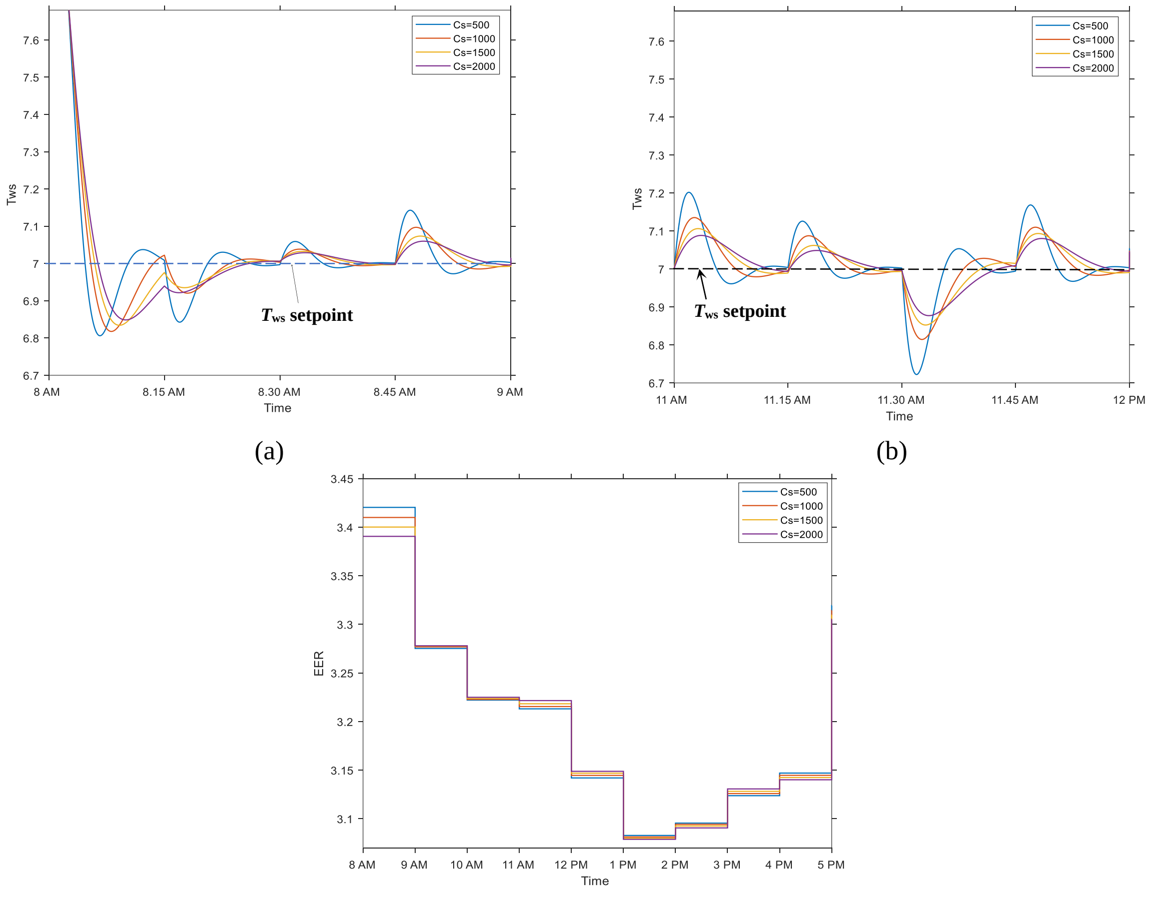

Figure 11. Variable-speed chiller results with different C_s values: (a) Water supply temperature profile from 8-9 am in the high cooling load day, (b) Water supply temperature profile from 11-12 am on the high cooling load day, and (c) EER values in the high cooling load day

The results of the sensitivity analysis for the case of the constant-speed chiller are presented in Figure 12. In this case, results for the same two hours (i.e., 8-9 am and 11-12 am) are presented not only for the high cooling day (Fig 12. a-b) but also for the case of low cooling day (Fig 12.c-d).

As shown in Fig. 12.a, for the high cooling load day, only effects of CMP 2 are shown, since as previously observed, CMP 1 is always ON. Worth noting that, as C_s increases (i.e., when the thermal inertia of the hydronic circuit increases) the number of cycling strongly reduces. Indeed, when passing from C_s= 500 kJ/°C to 1000 kJ/°C, the number of cycling “ON-OFF” for CMP 2 decreases, but it is almost near the threshold values in both hours (i.e., 12 cycles per hour). However, if C_s is increased up to 1500 kJ/°C the number of cycling falls below the threshold value.

Regarding the low-load cooling day (Fig 12.c-d), only results for CMP 1 are shown, since as previously observed, CMP 2 is always OFF. Note that C_s should be increased up to 1500 kJ/°C to maintain the number of cycling below the threshold (i.e., 12 cycles per hour). By looking at the *EER* values in Figs 12.b and 12.d, it can be noted that the variation of C_s has minimal impact on it. As in the case of variable-speed systems, these results suggest that for the case of the constant-speed chiller, variation in thermal inertia of the hydronic loop does not heavily affect its energy performance, but it can lead to unsafe operation of CMPs.

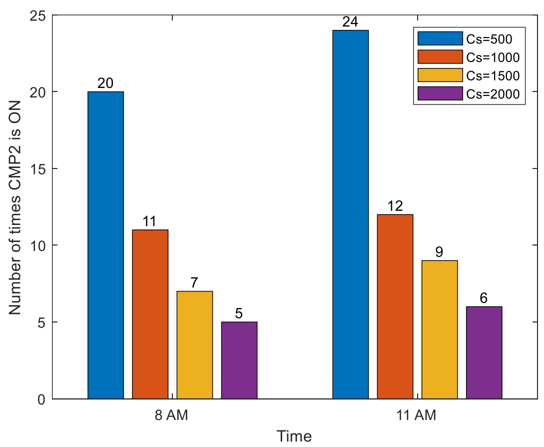

(a)

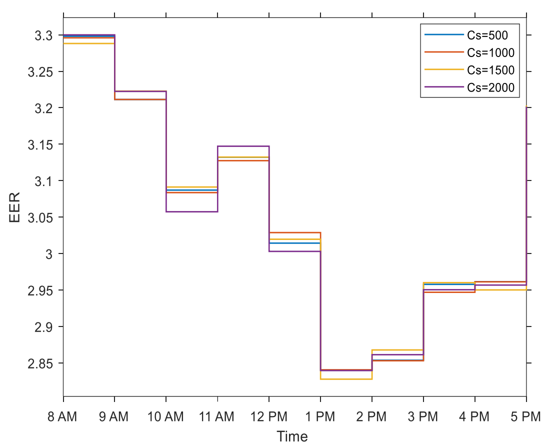

(b)

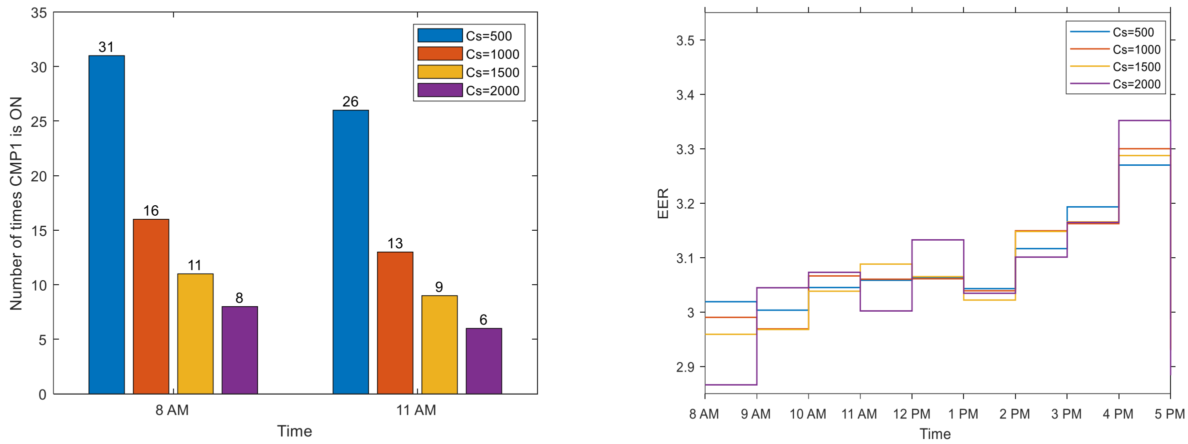

(c) (d)

Figure 12. Constant-speed chiller results with different C_s values: (a) Number of CMP 2 cycling in the high cooling load day, (b) *EER* values in the high cooling load day, (c) Number of CMP 1 cycling in the low cooling load day, and (d) *EER* values in the low cooling load day.

4.4 Flexible operation of the air-cooled chiller

In the proposed scenario, the chiller is operated by setting a variable setpoint for the temperature of the water supplied to the building, as shown in Figure 7. Results for the high cooling load day are shown in Figure 13.a-b. As shown in Fig. 13.a, the T_{ws} is not more kept at 7 °C like before (see Fig. 8-b). The values of T_{ws} vary from 8 °C in the early morning to around 7.4 °C from 10 to 12 am, since the *ODT* values are less than 30 °C till 12 am (see Fig. 5.a). As shown in Fig. 13.b, an increase in the average value in some hours is achieved by this new strategy (orange line) compared to the previous one (yellow line). In particular, from 8 to 9 am, the percentage increase of *EER* is 10.8% (from 3.42 to 3.79) thanks to the higher setpoint. The percentage variation of *EER* gradually reduces during the day, reaching almost zero during high-load hours (i.e., after 12 pm)

Results for the low-cooling load day are shown in Figure 13.c-d. In this case, since *ODT* is always less than 30 °C (as shown in Fig. 5.a.). Therefore, the water is supplied to a T_{ws} value higher than 7 °C (here T_{ws} ranges between 9 and 9.5 °C), with a substantial increase in the average *EER* value throughout the day (Fig. 13.d). In particular, the highest percentage variation in *EER* is observed from 4 to 5 pm (almost 60.3%), when the *EER* increases from about 3.9 to 6.25. Conversely, the minimum variation was found from 1 to 2 pm (almost 37.8%) when the *EER* increases from about 3.7 to 5.1.

These results suggested that the proposed strategy could be a promising solution to achieve a reduction in the electricity demanded by the chiller to the grid, which could be very helpful in evaluating the feasibility and effectiveness of demand response programs.

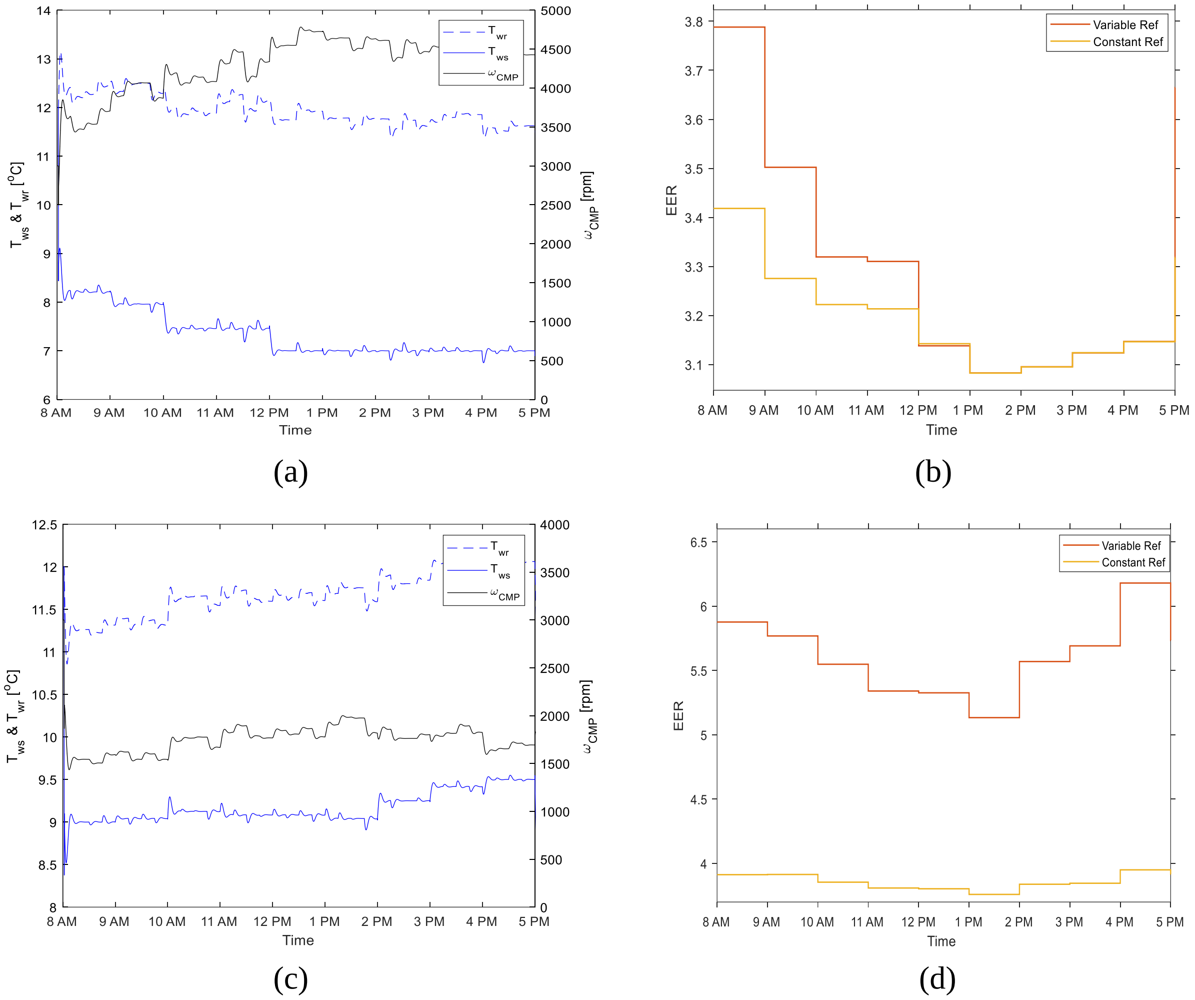

Figure 13. Results with sliding water supply temperature: (a) Water supply, Water return temperature, and CMP speed in the high cooling load day; (b) *EER* values in the high cooling load day; (c) Water supply, Water return temperature, and CMP speed in the low cooling load day; (d) *EER* values in the low cooling load day.

5. Conclusions

In this paper, an integrated thermodynamic and control modeling for an air-cooled chiller is developed to simulate the control strategies typically adopted in the field to meet the variable cooling demand and to test innovative ones aimed at increasing energy efficiency. To show the capabilities of the model, a variable-speed air-cooled chiller serving an office in the Mediterranean area is assumed as the case study. Results show that in the case of a variable-speed chiller, the model allows for continuous monitoring of the effect of controller action on the unit (e.g., the instantaneous values of CMP speed, IM torque, and the temperature of the cold water supplied to the building). Moreover, the required supply water setpoint is always met. In the case of a constant-speed chiller with sequential control for CMPs, a clear picture of the number of CMP cycling is provided, allowing for safety assessment during the chiller's operation. The model enables the possibility to perform sensitivity analyses of results with the design of the hydronic loop. In the case of a constant-speed chiller, the sensitivity analysis reveals that thermal inertia heavily affects the number of CMP cycling. In addition, the minimum thermal inertia value which allows keeping the CMP cycling below the threshold value is determined. Conversely, in the case of a variable-speed system, effects in terms of supply water temperature oscillation and overshot are estimated. Thanks to the proposed model, an innovative operating strategy is simulated. In this respect, it is found that room for energy savings existed when a sliding water supply temperature setpoint is adopted. In particular, the highest percentage variation in *EER* is observed on a day of low cooling demand (almost 60.3%). However, rooms of energy savings exist also on days of high cooling demand, where a 10.8% increase in the *EER* value could be achieved. As major implications in the field, the proposed study confirms the importance of a detailed thermodynamic and control modeling of chillers for the assessment of energy savings achievable through the adoption of innovative operating strategies. In this regard, modeling the dynamic response of chillers is crucial to quantify the time required and the energy consumed in reaching a steady-state operation after any change in boundary or loading conditions. Such dynamic modeling reveals extremely precious for a reliable assessment of the performance of chillers in handling demand-response programs and providing ancillary services in areas characterized by high penetration of intermittent renewables. In the current scenario where a large spread of hydronic reversible heat pumps is expected soon (representing key technologies for the ongoing replacement of gas boilers), assessing the effects of the thermal inertia of these units, when operated in cooling mode as chillers, and their hydronic loops, as well as the influence of the control strategy, on the time profile of power absorption, will be relevant for rational decision-making concerning power-dispatching by grid operators. Finally, integrated modeling of the chiller and the controller's action will be essential to guarantee strict respect for safety constraints regarding the frequency of CMP cycling, thus preventing the risk that innovative energy-saving-oriented control strategies could result in highly unstable operation and more frequent troubleshooting or reduced technical life expectancy of chillers. In future studies, the proposed integrated model will be further implemented focusing the attention on improved building flexibility.

Acknowledgments

This study was developed in the framework of the research activities carried out within the PRIN 2020 project: “OPTIMISM—Optimal refurbishment design and management of small energy micro-grids”, funded by the Italian Ministry of University and Research (MUR).

Acronyms

CMP	Compressor
CND	Condenser
CTRL	Control
EVP	Evaporator
EV	Expansion Valve
IM	Induction Motor
PI	Proportional and Integrator
RES	Renewable Energy Source
RMS	Root Mean Square
SHR	Sensible Heat Ratio
SC	Sequential control
SVM	Space vector modulation
VFD	Variable frequency drive
VSI	Voltage Source Inverter

Variables

CL	Building Cooling Load (W)
CC	Cooling Capacity (W)
V_{des}	Desired volume of water in the hydronic loop (m^3)
T_{el}	Electromagnetic torque (Nm)
EER	Energy Efficiency Ratio (dimensionless)
u_{s}	Input stator voltage (V)
$D_{\mathrm{a,b,c}}$	Inverter duty cycles (sec)
$\dot{m}_{\mathrm{w}}$	Mass flowrate of water circulating in the hydronic loop (kg/s)
P_{m}	Mechanical Power (W)
T_{L}	Mechanical torque (Nm)
L_{m}	Mutual inductance (H)
CC_{nom}	Nominal cooling capacity delivered (W)
NRMSE	Normalized Root Mean Square Error Index
p	Number of pair poles (dimensionless)
ODT	Outdoor air temperature (°C)
$T_{\mathrm{ws,ref}}$	Reference Temperature of the water supplied to the hydronic loop (°C)
L_{r}	Rotor inductance (H)
T_{r}	Rotor time constant (sec)
c_{W}	Specific heat capacity of water (kJ/(kg °C))
i_{s}	Stator currents (A)
L_{s}	Stator inductance (H)
R_{s}	Stator resistance (Ω)
T_{wr}	Temperature of the water returning from the hydronic loop (°C)
T_{ws}	Temperature of the water supplied to the hydronic loop (°C)
$V_{\mathrm{a,b,c}}$	Three-phase voltages (V)

Greek Letters

φ_{r}'	Rotor fluxes (Wb)
ω_{CMP}	Compressor rotating speed (rpm)
σ	Blondel coefficient (dimensionless)
ρ_{w}	Density of water (kg/m^3)

References

[1] International Energy Agency (IEA). Space Cooling. 2022. Available at: https://www.iea.org/reports/space-cooling.

[2] International Energy Agency (IEA). World Energy Outlook. 2022. Available at: https://www.iea.org/reports/world-energy-outlook-2022.

[3] Dincer I, Rosen MA, Dincer I, Rosen MA. Chapter 7 – Renewable Energy-Based Building HVAC Systems. Exergy Analysis of Heating, Refrigerating and Air Conditioning, 2015, p. 279–308. https://doi.org/10.1016/B978-0-12-417203-6.00007-7.

[4] Kouropoulos GP. Review of the Capacity Control Capability of Commercial Air Conditioner Units with Variable Speed Compressor. International Journal of Air-Conditioning and Refrigeration 2016; 24:1630005. https://doi.org/10.1142/S2010132516300056.

[5] Bell IH, Groll EA. Air-side particulate fouling of microchannel heat exchangers: Experimental comparison of air-side pressure drop and heat transfer with plate-fin heat exchanger. Appl Therm Eng 2011; 31:742–9. https://doi.org/10.1016/j.applthermaleng.2010.10.019.

[6] Cuevas C, Lebrun J, Lemort V, Winandy E. Characterization of a scroll compressor under extended operating conditions. Appl Therm Eng 2010;30:605–15. https://doi.org/10.1016/j.applthermaleng.2009.11.005.

[7] Nair V. HFO refrigerants: A review of present status and future prospects. International Journal of Refrigeration 2021;122:156–70. https://doi.org/10.1016/j.ijrefrig.2020.10.039.

[8] Niu J, Zhou R, Tian Z, Zhu J, Lu Y, Ma J. Energy-saving potential analysis for a 24-hour operating chiller plant using the model-based global optimization method. Journal of Building Engineering 2023;69:106213. https://doi.org/10.1016/j.jobe.2023.106213.

[9] Chan KC, Wong VTT, Yow AKF, Yuen PL, Chao CYH. Development and performance evaluation of a chiller plant predictive operational control strategy by artificial intelligence. Energy Build 2022;262:112017. https://doi.org/10.1016/j.enbuild.2022.112017.

[10] Catrini P, Piacentino A, Cardona F, Ciulla G. Exergoeconomic analysis as support in decision-making for the design and operation of multiple chiller systems in air conditioning applications. Energy Convers Manag 2020;220:113051. https://doi.org/10.1016/j.enconman.2020.113051.

[11] Saloux E, Zhang K. Data-Driven Model-Based Control Strategies to Improve the Cooling Performance of Commercial and Institutional Buildings. Buildings 2023;13:474. https://doi.org/10.3390/buildings13020474.

[12] Fan C, Zhou X. Model-based predictive control optimization of chiller plants with water-side economizer system. Energy Build 2023;278:112633. https://doi.org/10.1016/J.ENBUILD.2022.112633.

[13] Ismaen R, El Mekkawy TY, Pokharel S, Al-Salem M. System requirements and optimization of multi-chillers district cooling plants. Energy 2022;246:123349. https://doi.org/10.1016/J.ENERGY.2022.123349.

[14] Zhang J, He W, Guo R, Li H, Liu S, Wei J, et al. Optimal thermal management on server cooling system to achieve minimal energy consumption based on air-cooled chiller. Energy Reports 2022;8:154–61. https://doi.org/10.1016/J.EGYR.2022.10.237.

[15] Qiu S, Li Z, Fan D, He R, Dai X, Li Z. Chilled water temperature resetting using model-free reinforcement learning: Engineering application. Energy Build 2022;255:111694. https://doi.org/10.1016/J.ENBUILD.2021.111694.

[16] Liu X, Huang B, Zheng Y. Control strategy for dynamic operation of multiple chillers under random load constraints. Energy 2023;270:126932. https://doi.org/10.1016/j.energy.2023.126932.

[17] Sun S, Shan K, Wang S. An online robust sequencing control strategy for identical chillers using a probabilistic approach concerning flow measurement uncertainties. Appl Energy 2022;317:119198. https://doi.org/10.1016/J.APENERGY.2022.119198.

[18] Alghamdi SM, Ajour MN, Abu-Hamdeh NH, Karimipour A. Using PCM for building energy management to postpone the electricity demand peak load and approving a new PID controller to activate alternative chiller. Journal of Building Engineering 2022;57:104884. https://doi.org/10.1016/J.JOBE.2022.104884.
[19] Yu FW, Chan KT. Improved energy performance of air cooled centrifugal chillers with variable chilled water flow. Energy Convers Manag 2008;49:1595–611. https://doi.org/10.1016/J.ENCONMAN.2007.12.009.
[20] Liao Y, Sun Y, Huang G. Robustness analysis of chiller sequencing control. Energy Convers Manag 2015;103:180–90. https://doi.org/10.1016/J.ENCONMAN.2015.06.060.
[21] Mathiesen BV, Lund H, Karlsson K. 100% Renewable energy systems, climate mitigation and economic growth. Appl Energy 2011;88:488–501. https://doi.org/10.1016/j.apenergy.2010.03.001.
[22] Fischer D, Madani H. On heat pumps in smart grids: A review. Renewable and Sustainable Energy Reviews 2017;70:342–57. https://doi.org/10.1016/j.rser.2016.11.182.
[23] Guarino S, Buscemi A, Ciulla G, Bonomolo M, lo Brano V. A dish-stirling solar concentrator coupled to a seasonal thermal energy storage system in the southern mediterranean basin: A cogenerative layout hypothesis. Energy Convers Manag 2020;222:113228. https://doi.org/10.1016/j.enconman.2020.113228.
[24] Quirosa G, Torres M, Soltero VM, Chacartegui R. Analysis of an ultra-low temperature district heating and cooling as a storage system for renewable integration. Appl Therm Eng 2022;216:119052. https://doi.org/10.1016/j.applthermaleng.2022.119052.
[25] Guelpa E, Verda V. Demand response and other demand side management techniques for district heating: A review. Energy 2021;219:119440. https://doi.org/10.1016/j.energy.2020.119440.
[26] Tina GM, Aneli S, Gagliano A. Technical and economic analysis of the provision of ancillary services through the flexibility of HVAC system in shopping centers. Energy 2022;258:124860. https://doi.org/10.1016/j.energy.2022.124860.
[27] Lu F, Yu Z, Zou Y, Yang X. Cooling system energy flexibility of a nearly zero-energy office building using building thermal mass: Potential evaluation and parametric analysis. Energy Build 2021;236:110763. https://doi.org/10.1016/J.ENBUILD.2021.110763.
[28] Mugnini A, Polonara F, Arteconi A. Energy flexibility curves to characterize the residential space cooling sector: The role of cooling technology and emission system. Energy Build 2021;253:111335. https://doi.org/10.1016/J.ENBUILD.2021.111335.
[29] Triolo RC, Rajagopal R, Wolak FA, de Chalendar JA. Estimating cooling demand flexibility in a district energy system using temperature set point changes from selected buildings. Appl Energy 2023;336:120816. https://doi.org/10.1016/J.APENERGY.2023.120816.
[30] Liu H, Cai J. Improved superheat control of variable-speed vapor compression systems in provision of fast load balancing services. International Journal of Refrigeration 2021;132:187–96. https://doi.org/10.1016/j.ijrefrig.2021.08.028.
[31] Clauß J, Georges L. Model complexity of heat pump systems to investigate the building energy flexibility and guidelines for model implementation 2019;255:113847. https://doi.org/10.1016/j.apenergy.2019.113847.
[32] Maier L, Schönegge M, Henn S, Hering D, Müller D. Assessing mixed-integer-based heat pump modeling approaches for model predictive control applications in buildings. Appl Energy 2022;326:119894. https://doi.org/10.1016/j.apenergy.2022.119894.
[33] IMST-Group Instituto de Ingeniería Energética Universidad Politécnica de Valencia. IMST-Art v. 4.0, 2021.
[34] MathWorks. MATLAB v. R2022b.
[35] Thibault Péan. Heat Pump Controls to Exploit the Energy Flexibility of Building Thermal Loads. Spinger; 2020.

[36] Patil A, Hjortland A, Cheng L, Dhillon P, Braun JE. Load-based Testing to Characterize the Performance of Variable-Speed Equipment. INTERNATIONAL REFRIGERATION AND AIR CONDITIONING CONFERENCE, 2018.

[37] Michele V, Diego D. Le Centrali Frigorifere, Editoriale Delfino, 2015. (in Italian).

[38] Kumar DM, Mudaliar HK, Cirrincione M, Mehta U, Pucci M. Design of a Fractional Order PI (FOPI) for the Speed Control of a High-Performance Electrical Drive with an Induction Motor. 2018 21st International Conference on Electrical Machines and Systems (ICEMS), 2018, p. 1198–202. https://doi.org/10.23919/ICEMS.2018.8549407.

[39] Cirrincione M, Pucci M, G. V. Power converters and AC electrical drives with linear neural networks. CRC Press; 2016.

[40] Piacentino A, Barbaro C. A comprehensive tool for efficient design and operation of polygeneration-based energy μgrids serving a cluster of buildings. Part II: Analysis of the applicative potential. Appl Energy 2013;111:1222–38. https://doi.org/10.1016/J.APENERGY.2012.11.079.

[41] Meteonorm: Meteonorm, Global Meteorological Database. 2015:Handbook part II: theory, version 7.1.7.201517.

[42] Blanco Castro J, Urchueguía JF, Corberán JM, Gonzálvez J. Optimized design of a heat exchanger for an air-to-water reversible heat pump working with propane (R290) as refrigerant: Modelling analysis and experimental observations. Appl Therm Eng 2005;25:2450–62. https://doi.org/10.1016/j.applthermaleng.2004.12.009.

[43] Trane. Conquest air-cooled chillers and heat pumps, Model CGAX/CXAX, 42-160 kW. Available at: https://www.trane.com/litweb/.

[44] Braun JE, Klein SA, Mitchell JW. Effectiveness models for cooling towers and cooling coils. Volume: 95, Part 2; Conference: 1989 ASHRAE annual meeting, Vancouver (Canada), 25-28 Jun 1989; Journal ID: ISSN 0001-2505.

[45] Sabiana. “Carisma” Fan Coils, 2022. Available at: https://www.sabiana.it/it/products/carisma-crc.